ELSEVIER

Journal of Fluids and Structures 23 (2007) 920–937

JOURNAL OF
FLUIDS AND
STRUCTURES

www.elsevier.com/locate/jfs

Estimating turbulent-boundary-layer wall-pressure spectra from CFD RANS solutions

L.J. Peltier*, S.A. Hambric

Applied Research Laboratory, The Pennsylvania State University, P.O. Box 30, State College, PA 16804, USA

Received 21 February 2005; accepted 2 January 2007

Abstract

A stochastic model for the space–time turbulent boundary-layer wall-pressure spectrum is developed that uses statistical data from Reynolds-Averaged Navier–Stokes (RANS) solutions as input. The model integrates the source terms for the surface-pressure covariance across the boundary layer for user-specified space and time separations to form a discrete surface-pressure correlation function, the Fourier transform of which yields the surface-pressure wavenumber-frequency spectrum. By integrating RANS data into the model, it is able to respond to local geometry and flow conditions. Validation cases show that predicted surface-pressure power spectra respond appropriately to favorable, zero, and adverse pressure gradients. By operating as a post-processor of CFD RANS analyses, the model is a predictive tool that can be used in flow and flow-induced noise analyses. Because contemporary RANS models are able to predict flow statistics well for configurations of practical interest, this approach to modeling the turbulent boundary-layer forcing function is expected to generalize well to new flow configurations without requiring flow-specific tuning.

---

1. Introduction

The bulk of research on the behavior of the velocity and pressure fluctuations within turbulent boundary layer (TBL) flows has been conducted under ideal conditions, such as on flows with zero pressure gradient over flat plates (Klebanoff, 1954), and inside cylinder (pipe) interiors (Laufer, 1954) and channels (Laufer, 1950). Estimates have been made by many authors of the wall-pressure autospectra and cross-spectra for a variety of flow speeds and fluid properties. The survey by Bull (1996) summarizes much of the existing research. The wall-pressure autospectra may be collapsed reasonably well using combinations of the so-called inner or outer flow variables, where outer variable scaling collapses low-frequency levels well, and inner variable scaling collapses high-frequency levels well. Keith et al. (1991) explored mixed variable scaling, where the frequency is scaled on outer variables and the pressure levels scaled on inner variables, and obtained good general collapse of levels over all frequencies.

Empirical models of wall-pressure autospectra under zero pressure gradient TBL flow have been proposed by several authors, such as Corcos (1963), Chase (1980, 1987) and Smolyakov and Tkachenko (1991), that are essentially curve fits to the scaled measured data sets. For example, Fig. 1 shows the model of Smolyakov and Tkachenko plotted against

---

*Corresponding author. Tel.: +1 814 863 3014; fax: +1 814 865 8896.

E-mail addresses: peltierlj@psu.edu (L.J. Peltier), sah19@only.arl.psu.edu (S.A. Hambric).

0889-9746/$ - see front matter © 2007 Elsevier Ltd. All rights reserved.
doi:10.1016/j.jfluidstructs.2007.01.003

Nomenclature

C^{ij}	2-point fluctuating velocity correlation function (SAM model)
C_f	skin-friction coefficient $(2(u_*/u_e)^2)$
f, g	isotropic turbulence functions (SAM model)
G	Green's function
i, j, k	indices
k	turbulence kinetic energy
k^+	turbulence kinetic energy in wall units
ℓ	turbulence length scale
ℓ^+	turbulence length scale in wall units
L_r	reference length for nondimensionalization
p	fluctuating pressure
P	mean pressure
q	turbulent kinetic energy
r, r^*	radius and effective radius (SAM model)
r_i	Cartesian coordinate of correlation space
$\vec{r}$	Cartesian coordinate of correlation space (vector form)
Re	Reynolds number from nondimensionalization $(U_r L_r/\nu)$
Re_δ	boundary-layer thickness Reynolds number $(u_e\delta/\nu)$
Re_*	displacement thickness Reynolds number $(u_*\delta_*/\nu)$
Re_θ	momentum thickness Reynolds number $(u_e\theta/\nu)$
R_{pp}	2-point wall-pressure correlation function
SRC	source term
t	time
TMS	turbulence–mean-shear interactions
TT	turbulence–turbulence interactions
TTM	turbulence normal-stress/shear-stress interactions
TTN	turbulence normal-stress/normal-stress interactions
TTS	turbulence shear-stress/shear-stress interactions
u_*	friction velocity
$\tilde{u}_i$	instantaneous velocity
u_c	convection velocity (SAM model)
u_e	boundary-layer edge velocity (velocity at δ)
u_i	fluctuating velocity
U_i	mean velocity
U_r	reference velocity for nondimensionalization
v_i	fluctuating velocity (2nd point)
V_i	mean velocity (2nd point)
x_i	Cartesian coordinate
$\vec{x}, \vec{x}_s$	Cartesian coordinates in space, and of surface point s (vector form)
$\Vert\vec{x}\Vert$	vector magnitude
x_{ref}	reference longitudinal coordinate (SAM model)
y^+	wall-normal coordinate in wall units
y_j	Cartesian coordinate (2nd point)
y_{ref}	reference wall-normal coordinate (SAM model)
$\vec{y}, \vec{y}_s$	Cartesian coordinates in space, and of 2nd surface point s (vector form)
z_{ref}	reference cross-stream coordinate (SAM model)
γ_i	stretching coefficients (SAM model)
δ	boundary-layer thickness
δ_*	boundary-layer displacement thickness
δ_{ij}	Kronecker delta
$\Delta\vec{x}$	spatial separation vector
$\Delta\vec{r}$	spatial separation vector in correlation space
Δt	separation time
θ	inclination angle (SAM model), boundary-layer momentum thickness
$\vec{\kappa}$	wave vector
Λ_f	turbulence correlation length (SAM model)
ν	kinematic diffusivity
$\vec{\xi}$	major/minor axes coordinate vector (SAM model)
ξ_i	major/minor axes coordinate (SAM model)
ρ	density
τ	time (2nd point)
τ_w	wall shear stress
Φ_{pp}	wavenumber-frequency spectrum, also radian-frequency spectrum
ω	radian frequency, inverse time scale for the $q-\omega$ turbulence model

several sets of measured data compiled by Keith et al. using mixed variable scaling. Since all pressure sensors attenuate high-wavenumber fluctuations over their surfaces to some degree, the well known Corcos correction (1963) is applied to the measurements shown in Fig. 1.

Empirical models are based on fits to data under ideal conditions. Given limited input data, they can be rescaled to estimate local wall-pressure autospectra. Real conditions, however, may differ greatly from the ideal ones used to develop the empirical descriptions. This fact motivates the thought that a physics-based approach that can tailor itself to the local flow environment may provide an improved predictive capability.

Computational Fluid Dynamics (CFD) tools are routinely used to simulate local flow conditions in geometrically complicated environments at high Reynolds numbers (UD/ν), where U and D are the characteristic velocity and length scales and ν is the kinematic viscosity. Flows past marine vehicles and through engines ($\mathrm{Re}\sim 10^9$) are examples. These solutions satisfy model equations that govern fluid flow; solving the Reynolds-Averaged Navier–Stokes (RANS)

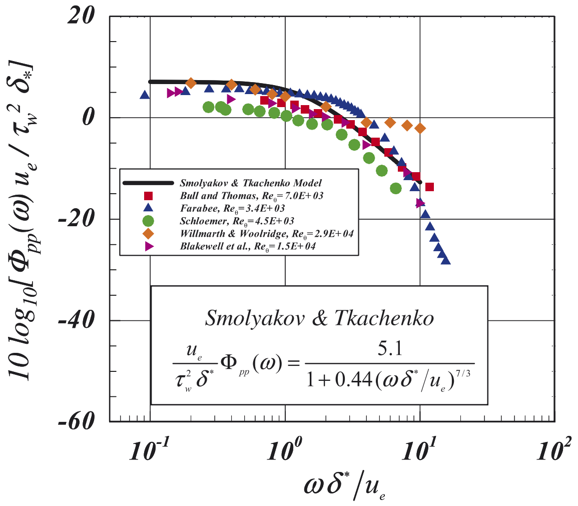

Fig. 1. Smolyakov and Tkachenko TBL wall-pressure autospectra model vs. measured data.

equation set is the contemporary production approach. CFD methods are very sophisticated and resolve explicitly some of the complicated nonlinear interactions that characterize fluid dynamics. CFD tools are now used routinely to guide sensitive engineering decisions, like safety measures for the space shuttle. We suggest that the additional fidelity to physics offered by CFD may be exploited to improved physics modeling of turbulent wall-pressure spectra.

We propose to integrate through the boundary-layer expressions for the surface-pressure space–time covariance. The approach requires closure with an empirical model for the space–time velocity correlation and the selection of an appropriate near-surface Green's function. The advantage of this approach is that it imposes a priori no structure on the predicted surface-pressure covariance function and associated wavenumber-frequency spectrum. The predicted statistics respond to non-ideal boundary layers induced by complicated local flow conditions.

Contributions from two main mechanisms—the interaction of turbulence with the mean-shear distribution in the flow field (TMS), and the interaction of turbulence with itself (TT) appear in the model. The model will be exercised on fully-developed channel flow with zero pressure gradient, then applied to internal-flow solutions from diverging and converging ducts with favorable and adverse pressure gradients. Simulations will be compared to measured data by Schloemer (1966, 1967). The relative importance of the TMS and TT terms in each type of flow will be shown.

2. TBL wall-pressure modeling

A common approach to developing contemporary models of the wall pressure autospectra due to TBL flow is to evolve an expression for the surface-pressure covariance incorporating progressively more restrictive modeling assumptions, see for example the formulations by Kraichnan (1956), Gardner (1965/1966), Meecham and Tavis (1980) and Blake (1986). The most restrictive assumptions generally involve closure of turbulence correlations within the forcing fluid. Without specific knowledge of general flow fields of interest, turbulence closures have relied on experimental data from simple geometries. Those data may not generalize well to non-trivial flow configurations.

RANS modeling is a computational technique that experience shows is able to provide predictions of the mean velocity and shear stress statistics of a flow field with reasonable fidelity, even for complicated geometries and flow conditions. Flow data and basic turbulence parameters are provided by RANS. That data yields local estimates of the expected flow variables specific to a particular geometry and a particular set of operating conditions.

The RANS data provide one-point velocity and turbulence statistics. Coupled with a model for the two-point velocity correlation, the RANS data can be used to guide a stochastic model for the surface-pressure space–time covariance and its Fourier-space counterpart, the surface-pressure wavenumber-frequency spectrum. The modeling approach and embedded closures for a new model for the surface-pressure forcing function are outlined below. We begin by deriving an exact expression for the surface-pressure covariance that includes terms to be modeled, then proceed to define reasonable models to close the expression. The modeling approach is guided by the goal to introduce single-point mean-flow statistics from a RANS solution as input.

2.1. The fluctuating-surface-pressure equation

An analytic solution for the fluctuating surface pressure can be formed by integrating the fluctuating pressure Poisson equation [see Chang et al. (1999), among others, for details] using an appropriate Green's function

$$\frac{1}{\rho}p(\vec{x}_s,t)=\int_{\vec{x}}-\frac{\partial\left(2U_iu_j+u_iu_j-\overline{u_iu_j}\right)}{\partial x_i\partial x_j}G(\vec{x},\vec{x}_s)\,\mathrm{d}\vec{x}. \tag{1}$$

Our convention represents mean field quantities in upper case and fluctuations in lower case. The overbar denotes ensemble averaging. Two types of terms are identified, those containing mean-shear interactions with turbulence and those representing turbulence interactions with itself

$$\frac{1}{\rho}p(\vec{x}_s,t)=\int_{\vec{x}}-\left[2\frac{\partial}{\partial x_i}\left(\frac{\partial U_i}{\partial x_j}u_j\right)G(\vec{x},\vec{x}_s)+\frac{\partial\left(u_iu_j-\overline{u_iu_j}\right)}{\partial x_i\,\partial x_j}G(\vec{x},\vec{x}_s)\right]\mathrm{d}\vec{x}. \tag{2}$$

The right-side of (2) contains derivatives of the source terms contributing to the instantaneous surface pressure weighted by an influence function (the Green's function). The reformulation of the first source term to depend on mean-shear rather than mean-velocity is motivated by the understanding that mean-shear production is the primary mechanism for turbulence generation in the turbulent-kinetic-energy budget.

For convenience, the spatial derivatives are moved from the source terms to the Green's functions via repeated applications of the divergence theorem

$$\frac{1}{\rho}p(\vec{x}_s,t)=\int_{\vec{x}}-\left[2\left(\frac{\partial U_i}{\partial x_j}u_j\right)\frac{\partial G(\vec{x},\vec{x}_s)}{\partial x_i}+\left(u_iu_j-\overline{u_iu_j}\right)\frac{\partial^2G(\vec{x},\vec{x}_s)}{\partial x_i\,\partial x_j}\right]\mathrm{d}\vec{x}. \tag{3}$$

This step allows the derivatives to be computed analytically for an analytic model for the Green's function and reduces the number of spatial gradients that must be computed from the discrete RANS data.

Eq. (3) can be interpreted as the response from a virtual probe sampling the instantaneous fluctuating-pressure field. To create a statistic that is tractable through stochastic modeling, a second virtual probe is required, giving the instantaneous fluctuating-pressure at a second point displaced in space and/or time

$$\frac{1}{\rho}p(\vec{y}_s,\tau)=\int_{\vec{y}}-\left[2\left(\frac{\partial V_k}{\partial y_l}v_l\right)\frac{\partial G(\vec{y},\vec{y}_s)}{\partial y_k}+(v_kv_l-\overline{v_kv_l})\frac{\partial^2G(\vec{y},\vec{y}_s)}{\partial y_k\,\partial y_l}\right]\mathrm{d}\vec{y}. \tag{4}$$

The change in notation from x to y and U to V denotes simply that the second point is independent of the first one.

2.2. The surface-pressure covariance model

A statistical expression for the surface-pressure covariance is formed from the ensemble-average of the product of (3) and (4)

$$\frac{1}{\rho^2}\overline{p(\vec{x}_s,t)p(\vec{y}_s,\tau)}=\int_{\vec{y}}\int_{\vec{x}}\left[\begin{array}{l}4\dfrac{\partial U_i\partial V_k}{\partial x_j\;\partial y_l}\overline{u_jv_l}\dfrac{\partial G(\vec{x},\vec{x}_s)\partial G(\vec{y},\vec{y}_s)}{\partial x_i\qquad\partial y_k}\\ \quad+2\overline{u_iv_ku_jv_l}\dfrac{\partial^2G(\vec{x},\vec{x}_s)\partial^2G(\vec{y},\vec{y}_s)}{\partial x_i\,\partial x_j\quad\partial y_k\,\partial y_l}\\ \quad+\left\{\left(\overline{u_iu_jv_kv_l}-\overline{u_iu_j}\,\overline{v_kv_l}-\overline{u_iv_k}\,\overline{u_jv_l}-\overline{u_iv_l}\,\overline{u_jv_k}\right)\right.\\ \quad\left.\times\dfrac{\partial^2G(\vec{x},\vec{x}_s)\partial^2G(\vec{y},\vec{y}_s)}{\partial x_i\,\partial x_j\quad\partial y_k\,\partial y_l}\right\}\\ \quad-\left\{2\dfrac{\partial U_i}{\partial x_j}\overline{u_jv_kv_l}\dfrac{\partial G(\vec{x},\vec{x}_s)\partial^2G(\vec{y},\vec{y}_s)}{\partial x_i\qquad\partial y_k\,\partial y_l}\right\}\\ \quad-\left\{2\dfrac{\partial V_k}{\partial y_l}\overline{u_iu_jv_l}\dfrac{\partial G(\vec{y},\vec{y}_s)\partial^2G(\vec{x},\vec{x}_s)}{\partial y_k\qquad\partial x_i\,\partial x_j}\right\}\end{array}\right]\mathrm{d}\vec{x}\,\mathrm{d}\vec{y}. \tag{5}$$

The terms in (5) are grouped by interaction type. The 1st, 4th, and 5th groups on the right-side of (5) represent interactions between turbulence stresses and mean shear (TMS). The 2nd and 3rd groups are turbulence interactions with turbulence (TT).

The 3rd, 4th, and 5th groups, in braces, are zero, if the fluctuating velocity field at a point satisfies a normal probability distribution: the 3rd group because the 4th-order moment in the cumulant tensor can be written as products of 2nd-order moments and the 4th and 5th groups because odd-order moments are zero for symmetric distributions. A turbulence field cannot satisfy exactly a normal distribution, but for homogeneous turbulence and for turbulence near the center of a shear flow, the probability distribution for the fluctuating velocity field is nearly normal (Townsend, 1980, p. 128). Neglecting these terms, the final surface-pressure covariance expression to be modeled is

$$\frac{1}{\rho^2}\overline{p(\vec{x}_s,t)p(\vec{y}_s,\tau)} = \int_{\vec{y}}\int_{\vec{x}} \left[\begin{array}{l} 4\dfrac{\partial U_i}{\partial x_j}\dfrac{\partial V_k}{\partial y_l}\overline{u_j v_l}\dfrac{\partial G(\vec{x},\vec{x}_s)}{\partial x_i}\dfrac{\partial G(\vec{y},\vec{y}_s)}{\partial y_k} \\ \quad +2\overline{u_i v_k u_j v_l}\dfrac{\partial^2 G(\vec{x},\vec{x}_s)}{\partial x_i\,\partial x_j}\dfrac{\partial^2 G(\vec{y},\vec{y}_s)}{\partial y_k\,\partial y_l} \end{array} \right] \mathrm{d}\vec{x}\,\mathrm{d}\vec{y}. \tag{6}$$

The right-side of (6) requires knowledge of the mean-shear field, of the two-point fluctuating-velocity correlation function, and of an appropriate Green's function. The mean shear can be diagnosed from RANS. Models are required for the two-point fluctuating-velocity correlation function and for the Green's function. We recognize that wall-bounded flows can support skewed statistics that may not support some of the simplifying assumptions that lead to Eq. (6). The final success of this development, therefore, will rest on the comparisons between model predictions and measurements.

The two-point velocity correlation (of u_i and v_k) can be written as the product of a one-point velocity correlation (of u_i and u_k from RANS) and a spatially and temporally varying correlation coefficient

$$\overline{u_i v_k} \equiv \overline{u_i u_k}\, C^{ik}. \tag{7}$$

For a statistically stationary flow field, the only dependence of the surface-pressure covariance on time enters through the time dependence of the correlation coefficient.

The mean-shear values in (6) are from separated points in the flow field. Thus, knowledge of the 3-D mean-shear statistic is required. A convenient (but not necessary) simplification to (6) is achieved by recognizing that the correlation function is significant only within a bounded correlation volume. If the mean-shear varies slowly over this correlation space, the mean-shear contribution is effectively a one-point quantity

$$\frac{\partial V_k}{\partial y_l} \approx \frac{\partial U_k}{\partial x_l}. \tag{8}$$

The practical advantages of (7) and (8) are that (i) they introduce an explicit dependence of the source terms on RANS data and (ii) they limit the extraction of the required RANS data to a common point in the mean flow field. Also, the correlation space is the natural coordinate frame for the inner integral in (6), because the RANS data are approximately constant within it. An explicit dependence on correlation space can be introduced by the transform of coordinates from $(\vec{x},\vec{y})$ to $(\vec{x},\vec{r})$, where $\vec{r}=\vec{y}-\vec{x}$. Substituting (7) and (8) into (6) and transforming coordinates, we have

$$\frac{1}{\rho^2}\overline{p(\vec{x}_s,t)p(\vec{y}_s,\tau)} = \int_{\vec{x}}\int_{\vec{r}} \left[\begin{array}{l} 4\dfrac{\partial U_i}{\partial x_j}\dfrac{\partial U_k}{\partial x_l}\overline{u_j u_l}C^{jl}\dfrac{\partial G(\vec{x},\vec{x}_s)}{\partial x_i}\dfrac{\partial G(\vec{r},\vec{x},\vec{y}_s)}{\partial r_k} \\ \quad +2\overline{u_i u_k u_j u_l}C^{ik}\,C^{jl}\dfrac{\partial^2 G(\vec{x},\vec{x}_s)}{\partial x_i\,\partial x_j}\dfrac{\partial^2 G(\vec{r},\vec{x},\vec{y}_s)}{\partial r_k\,\partial r_l} \end{array} \right] \mathrm{d}\vec{r}\,\mathrm{d}\vec{x}. \tag{9}$$

The practical advantage of using (9) is that the inner integral will converge within a limited subvolume in space, a desirable characteristic for discrete integration.

Evaluation of (9) requires the computation of a large number of terms, many with negligible contribution. The number can be reduced considerably by retaining only those terms which contribute to boundary-layer flows at high Reynolds number. If the boundary-layer thickness is much smaller than the local radius of curvature of the geometry, the boundary layer will resemble a flat-plate boundary layer whose mean-flow statistics vary rapidly only in the wall-normal direction and Reynolds-stresses are the three energy terms and one shear-stress term

$$U_i(\vec{x}) \approx U(y) \quad \text{and} \quad \overline{u_i u_j}(\vec{x}) \in \left\{\overline{u_1u_1}(y),\ \ \overline{u_2u_2}(y),\ \ \overline{u_3u_3}(y),\ \ \overline{u_1u_2}(y)\right\}. \tag{10}$$

The Reynolds stresses in (10) are one-point statistics. In retaining only these correlations, we risk losing terms that become nonzero for nonzero separations. They are believed to be small, however, we note that this step may be a source of model error. Again, the final success of the finished model must be evaluated by comparisons to measurements.

Simplifying (10) with (9), the surface-pressure covariance equation becomes

$$\frac{1}{\rho^2}\overline{p(\vec{x}_s,t)p(\vec{y}_s,\tau)} = \int_{\vec{x}}\int_{\vec{r}}\left[\begin{array}{l} 4\dfrac{\partial U\partial U}{\partial y\;\partial y}\overline{u_2u_2}C^{22}\dfrac{\partial G(\vec{x},\vec{x}_s)\partial G(\vec{r},\vec{x},\vec{y}_s)}{\partial x\qquad\quad \partial r_1} \\ \quad +2\overline{u_iu_ku_ju_l}C^{ik}C^{jl}\dfrac{\partial^2 G(\vec{x},\vec{x}_s)\partial^2 G(\vec{r},\vec{x},\vec{y}_s)}{\partial x_i\,\partial x_j\qquad \partial r_k\,\partial r_l} \end{array}\right]\mathrm{d}\vec{r}\,\mathrm{d}\vec{x}. \tag{11}$$

The boundary-layer assumption isolates in (11) only one *TMS* contribution as dominant. It depends on the C^{22} correlation function. The identification of this term as the *TMS* partial-pressure contribution agrees with Chang et al.'s (1999) definition.

A number of TT contributions remain. They can be classified as turbulence normal-stress/normal-stress interactions (TTN), mixed turbulence normal-stress/shear-stress interactions (TTM), and turbulence shear-stress/shear-stress interactions (TTS). Here we depart from Chang et al. (1999). The current model-development transfers the derivatives from the source terms to the Green's functions, whereas Chang et al. (1999) distribute the spatial derivatives within the source terms. Consequently, their TT partial pressures are difficult to associate directly with the apparent partial pressures from (11). A notable difference is the absence of the cross-stream contributions to the Reynolds stresses in (10). The $\overline{uw}$ and $\overline{vw}$ stresses are zero. Chang et al.'s (1999) partial pressures containing the w component of the fluctuating velocity are dominant at low frequencies and wavenumbers. Chang et al. (1999) document strong cancellations among their partial-pressure source terms in the low frequency/wavenumber range. Their total spectrum is attenuated relative to the separate partial-pressure contributions. A similar observation is reported by Kim (1989) who shows that although the pressure field in an incompressible flow is elliptic, contributions to the mean-square statistic are local. The distant terms, contributing to the low frequency/wavenumber range, cancel in forming the statistic. By writing (11) in terms of the Reynolds stresses, not in terms of gradients of the fluctuating velocities [like Chang et al. (1999)], we may have accommodated much of the observed cancellation. This conjecture is worthy of further investigation in a separate work.

Although written in terms of four independent variables, the pressure covariance is assumed to be a function only of the space, $\Delta\vec{x} = \vec{x}_s - \vec{y}_s$, and time, $\Delta t = t - \tau$, separation

$$\frac{1}{\rho^2}\overline{p(\vec{x}_s,t)p(\vec{y}_s,\tau)} \equiv \frac{1}{\rho^2}\overline{p(\Delta\vec{x},\Delta t)p(0,0)} \equiv \frac{1}{\rho^2}R_{pp}(\Delta\vec{x},\Delta t). \tag{12}$$

The spatial separation vector lies in the plane of the wall and has components in the stream-wise and cross-stream directions. Expression (11) provides a governing equation for the surface-pressure covariance whose source terms use RANS data as input. To close the expression, models for the turbulence-velocity correlation functions and for the Green's functions must be chosen.

2.3. Green's-function modeling

The use of the boundary-layer approximation (10) motivates using the flat-plate Green's function to close (11). The flat-plate Green's function states that the influence of a volumetric source term decays as the inverse distance to the surface point

$$G(\vec{x},\vec{x}_s) \approx -\frac{1}{2\pi}\frac{1}{\|\vec{x}-\vec{x}_s\|}. \tag{13}$$

Note that we apply this Green's function to all source terms in the boundary layer, regardless of their size and decay times. Also, we do not consider compressibility in our formulation. Expression (11) uses the first and second derivatives of the Green's function. Analytic expressions for these derivatives are

$$\frac{\partial G(\vec{x},\vec{x}_s)}{\partial x_i} \approx \frac{1}{2\pi}\frac{\|x_i - x_{is}\|}{\|\vec{x}-\vec{x}_s\|^3} \quad \text{and} \quad \frac{\partial^2 G(\vec{x},\vec{x}_s)}{\partial x_i\,\partial x_j} \approx \frac{1}{2\pi}\left[\frac{\delta_{ij}}{\|\vec{x}-\vec{x}_s\|^3} - 3\frac{\|(x_i - x_{is})(x_j - x_{js})\|}{\|\vec{x}-\vec{x}_s\|^5}\right]. \tag{14}$$

The remaining function to be modeled is the turbulence-velocity correlation function.

2.4. Modeling the turbulence-velocity correlation function

As noted, the turbulence-velocity correlation function is the sole term in (11) that depends on time; so, the surface-pressure covariance model will be sensitive to the fidelity of the model for this function. The desired model must be appropriate for turbulent boundary-layer flow.

Gavin (2002) performed detailed surveys of the turbulence velocity correlations in the outer parts of a high-Reynolds number boundary layer. He presents contours for the turbulence velocity correlations for separations in the cross-stream and wall-normal directions and in time. The stream-wise dependence can be inferred from the temporal dependence assuming Taylor's frozen flow hypothesis.

Gavin (2002) presents two empirical models tuned to fit his data. One, the Simplified Anisotropic Model (SAM), is adopted as the turbulence velocity-correlation closure for (11). Gavin's measurements show that a turbulence-velocity correlation volume can be modeled as an ellipsoid inclined at an angle θ to the wall (see Fig. 2). From his measurements, he extracts estimates of the inclination angle and of the stretching relationships between the major and minor axes of the ellipsoid.

Gavin's SAM modeling approach is to use the measured data to define a mapping of the ellipsoid onto a sphere, then to apply isotropic turbulence relations to model the correlation data. The transformation begins with the magnitude of the space/time separation vector between the correlated points

$$r = \sqrt{((x - x_{\mathrm{ref}}) + u_c \Delta t)^2 + (y - y_{\mathrm{ref}})^2 + (z - z_{\mathrm{ref}})^2}. \tag{15}$$

Gavin rotates this separation into the major/minor-axis coordinate frame of the ellipsoid

$$\vec{\xi} = \begin{bmatrix} \cos(\theta) & -\sin(\theta) & 0 \\ \sin(\theta) & \cos(\theta) & 0 \\ 0 & 0 & 1 \end{bmatrix} \begin{bmatrix} (x - x_{\mathrm{ref}}) + u_c \Delta t \\ y - y_{\mathrm{ref}} \\ z - z_{\mathrm{ref}} \end{bmatrix}, \tag{16}$$

then scales the major/minor coordinate axes onto the axes of a sphere. The correlation values in the transformed space depend only on the effective radius

$$r^* = \sqrt{\left(\frac{\xi_1}{\gamma_1}\right)^2 + \left(\frac{\xi_2}{\gamma_2}\right)^2 + \left(\frac{\xi_3}{\gamma_3}\right)^2}. \tag{17}$$

The stream-wise dependence assumes Taylor's frozen flow. Gavin's measurements allowed him to identify a convection velocity, u_c, to use in (15). His other model parameters were tuned to fit the data.

Using the radius given by (17), Gavin invokes the classical formulae for the velocity correlation functions in an isotropic flow

$$C^{ij}(\xi_1, \xi_2, \xi_3) = \frac{\xi_i \xi_j}{r^{*2}}[f(r^*) - g(r^*)] + \delta_{ij} g(r^*), \tag{18a}$$

where

$$f(r^*) = \exp\left(-\frac{r^*}{\Lambda_f}\right) \quad \text{and} \quad g(r^*) = \left(1 - \frac{r^*}{2\Lambda_f}\right) f(r^*). \tag{18b}$$

The scalar Λ_f is the correlation length. Table 1 presents a summary of the model parameters reported by Gavin and those modifications needed to use the SAM approach in (11).

Gavin's model is designed for the outer parts of the boundary layer and yield the anisotropy observed there. The model for the surface-pressure covariance, though, integrates across the entire boundary layer and requires a model for

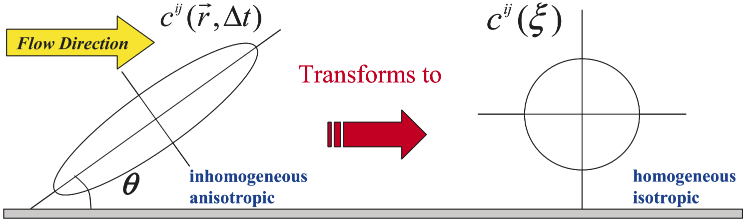

Fig. 2. Gavin's mapping of an ellipsoidal correlation volume onto a spherical one.

Table 1
SAM model coefficients reported by Gavin and those used in our model

	θ	γ_1	γ_2	γ_3	Λ_f (Gavin)	Λ_f (TBLFF)	u_c (Gavin)	u_c (TBLFF)
C^{11}	20	1.000	0.700	0.520	0.35δ	ℓ (RANS)	$0.7u_{\text{ref}}$	$0.7u_{\text{ref}}$
C^{12}	90	0.500	0.525	0.350	0.35δ	ℓ (RANS)	$0.7u_{\text{ref}}$	$0.7u_{\text{ref}}$
C^{13}	35	0.800	0.220	0.40	0.35δ	ℓ (RANS)	$0.7u_{\text{ref}}$	$0.7u_{\text{ref}}$

the turbulence-velocity correlation in regions where Gavin's SAM model does not apply. To use the SAM approach in the inner and intermediate parts of the boundary layer, we adopt his model coefficients that define the geometry and inclination of the correlation ellipsoid but use local values for the turbulence correlation length and for the "local" convection velocity.

Gavin's convection velocity was 70% of the velocity in the outer flow. It represents an average of the velocity across the boundary layer. A convection velocity is not needed to integrate (11), the local mean velocity is known, however, because Gavin's model parameters were tuned to his convection velocity, the 70% scaling of the local mean velocity had to be retained in the local SAM for it to agree with Gavin in the outer flow. To improve this approach, additional measurements are needed that yield appropriate model parameters as functions of the y^+ wall coordinate.

The SAM model does not provide a fit for the C^{12} correlation function. To evaluate its effects, we use the expression $C^{12} \approx \sqrt{C^{11}C^{22}}$ as our model.

In Fig. 3, we present separation-time contours of the SAM-modeled correlation functions, and contours for spatial separations in Fig. 4. These data reproduce the data presented by Gavin. Of note, the correlation volume in time and in the streamwise direction is large for the C^{11} component relative to the other components. Both C^{11} and C^{33} are elongated in time and the streamwise direction. The C^{22} component lacks this elongation and exhibits a markedly smaller correlation volume relative to C^{11}. Gavin presents a detailed discussion motivating that the boundary layer physics depends on coherent hairpin vortices. His Appendix D presents a model for the two-point correlation tensor based on a model for these coherent structures. His model produces a result that the C^{11} and C^{33} statistics are elongated in the flow direction, whereas the C^{22} statistic is not, yielding support to the thought that hairpin-like coherent structures are responsible for the dominant boundary layer physics.

The implications of the correlation function forms presented in Fig. 3 are that the turbulence–mean-shear contributions, which depend solely on C^{22}, will have a different character than the turbulence–turbulence contributions. Also, because the C^{11} and C^{33} terms are elongated in the streamwise direction and in time, the turbulence–turbulence terms will show a directional preference. The comparatively larger correlation volume for the C^{11} component also suggests that those terms depending on C^{11} remain significant for larger space and longer time separations.

Gavin's data fits have the most fidelity at small separations, within one correlation length. The modeling error increases with increasing separation. Our implementation of the SAM model restricts its use to within one correlation length where the model fidelity is highest.

2.5. *The wavenumber-frequency spectrum*

The wavenumber-frequency spectrum is the Fourier transform of the covariance function

$$\frac{1}{\rho^2}\Phi_{pp}(\vec{\kappa},\omega) = \frac{1}{(2\pi)^3}\int_{-\infty}^{\infty}\int_{-\infty}^{\infty}\int_{-\infty}^{\infty}\exp(-\mathrm{i}(\vec{\kappa}\vec{x}+\omega\Delta t))\frac{1}{\rho^2}R_{pp}(\vec{x},\Delta t)\,\mathrm{d}\vec{x}\,\mathrm{d}\Delta t. \tag{19}$$

It provides the complete turbulence boundary-layer forcing. Validation data in the literature for the wavenumber-frequency spectrum under variable pressure gradients is sparse. Notably, Schloemer (1966, 1967) presents data for favorable, zero, and adverse pressure gradients. Cipolla and Keith (2000) extended Schloemer's analysis to the wavenumber-frequency spectrum. Their results for the distribution of energy over the streamwise wavenumber at a fixed frequency, showed dropouts at discrete wavenumbers. These dropouts resulted from the limited data available to model the convection velocity for that particular experiment.

Schloemer's experimental data will be used to partially validate the surface-pressure covariance model (11). Schloemer measured the surface-pressure frequency spectrum defined by

$$\frac{1}{\rho^2}\Phi_{pp}(\omega) = \frac{1}{2\pi}\int_{-\infty}^{\infty}\exp(-\mathrm{i}\omega\Delta t)\frac{1}{\rho^2}R_{pp}(\vec{0},\Delta t)\,\mathrm{d}\Delta t \tag{20}$$

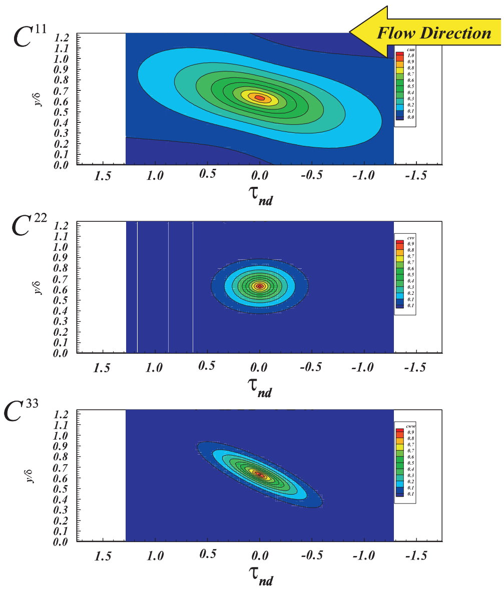

Fig. 3. Contours of Gavin's SAM C^{11}, C^{22}, and C^{33} correlation function model for separations in the wall-normal coordinate direction, y, and time, τ.

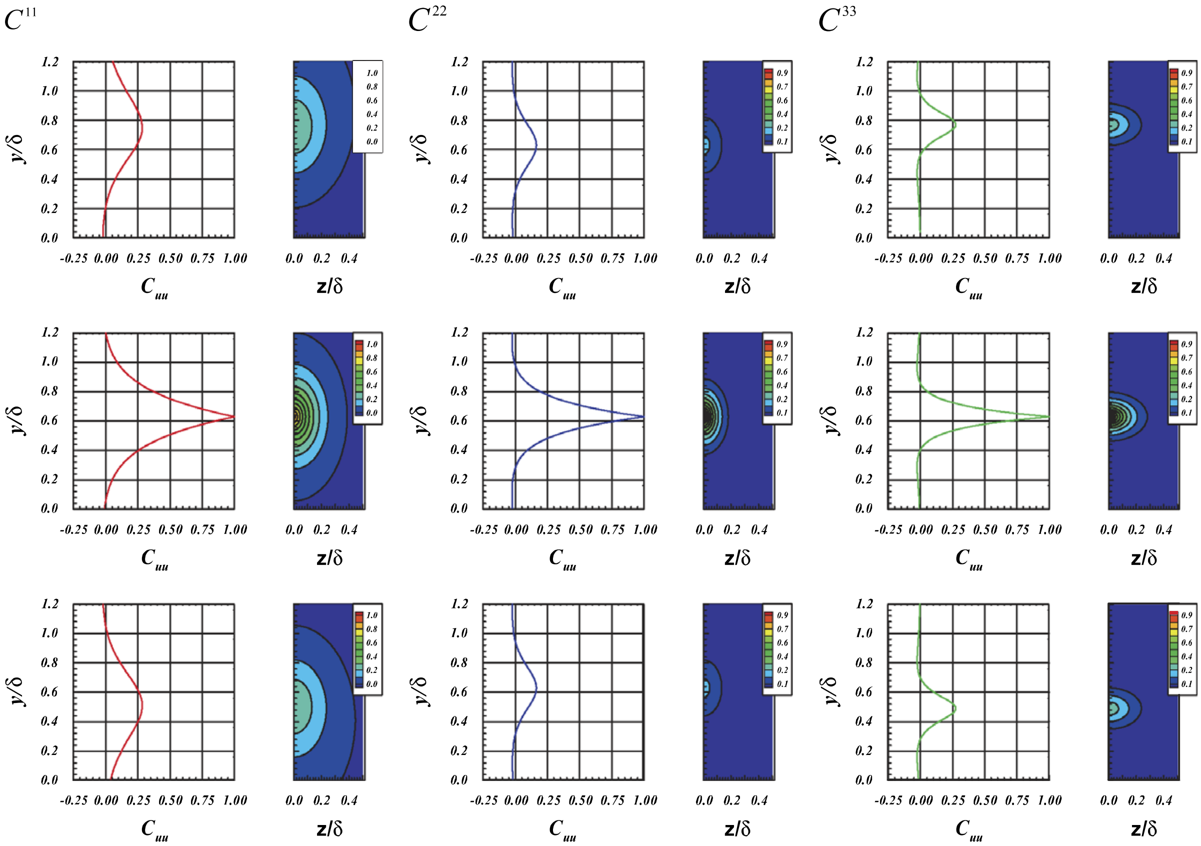

Fig. 4. Vertical profiles and contours in the wall-normal, y, and cross-stream, z, coordinate directions of Gavin's SAM C^{11}, C^{22}, and C^{33} correlation function models.

which is the Fourier transform of the covariance function at zero spatial separation, $\Delta\vec{x} = \vec{0}$. The surface-pressure temporal covariance is recovered from the frequency spectrum through its inverse transform

$$\frac{1}{\rho^2} R_{pp}(\vec{0}, \Delta t) = \int_{-\infty}^{\infty} \exp(\mathrm{i}\omega\Delta t) \frac{1}{\rho^2} \Phi_{pp}(\omega)\, \mathrm{d}\omega. \tag{21}$$

A similar expression can be written relating the surface-pressure wavenumber-frequency spectrum to the space–time covariance function. In future papers, we hope to validate the entire space–time covariance function.

3. Wall-pressure-model validation

The modeled surface-pressure autospectrum (20) does not impose directly the shape or the amplitude on the predicted profile. In this sense, it is very different from other contemporary models that attempt to build a spectrum model around the best fit to experimental data (Goody, 2002). A functional dependence on boundary-layer parameters and on pressure gradient can be designed into such models but it would be difficult to expect them to perform with fidelity under the very large range of flow and configuration conditions that are encountered in practice.

To compare to Schloemer (1966, 1967), RANS solutions must be generated that match approximately his favorable, zero, and adverse pressure gradient cases. Schloemer collected his experimental data in a wind tunnel in which he could vary the flow speed and the wall geometry. By mounting airfoil sections on the upper wall, he was able to create favorable and adverse pressure gradients. One approach to reproducing Schloemer's data is to emulate his geometry and flow conditions. Our modeling effort along this track did not yield an improved agreement with his reported boundary layer parameters over a simpler approach with a model geometry. Therefore, we chose to pursue a simpler method.

3.1. The RANS solution

To generate RANS data similar to Schloemer's results, a numerical experiment is constructed that provides adverse, approximately-zero, and favorable pressure-gradient regions. A schematic of the RANS domain is shown in Fig. 5. The diagram is not to-scale. The geometry consists of an entrance channel, a diffuser, a recovery channel, a contraction, and an exit channel in serial. The Reynolds number of the computation is 7×10^4, based on the entrance channel half height and on its centerline velocity. The dimensionless entrance channel length is 300 with height 2. This domain size ensures that the flow entering the diffuser is fully developed. The diffuser rise is 8.7 over a length of 100. The recovery section height is 10.7 extending a distance of 1700. The duct contracts a height of 8.7 over a length of about 100 to return to fully-developed channel flow in a duct of height 2 and length 200. The first and last stages of the RANS domain are used to separate the inflow and outflow boundaries from the nearest measurement stations to minimize their impact on the extracted data.

The computational domain is an internal flow, so drag losses must be overcome by a mean pressure drop. The deviation-pressure gradient is zero in this section. The flow conditions and data extraction locations are chosen to be consistent with Schloemer. We looked for consistent Reynolds numbers based on momentum thickness—7000–9000 for the adverse pressure gradient profiles, near 1400 for the favorable pressure gradient profiles, and near 5000 for the zero pressure profiles—and similar shape factors. This Reynolds number range is not the limit of our model. RANS solutions for boundary layers at much higher Reynolds numbers are routinely computed. For example, computations for flows around ships have Reynolds numbers of order 10^9 giving a momentum thickness Reynolds number of order 10^6. Such Reynolds numbers exceed considerably the Reynolds numbers that can be achieved with DNS or other boundary-layer-resolving CFD methods.

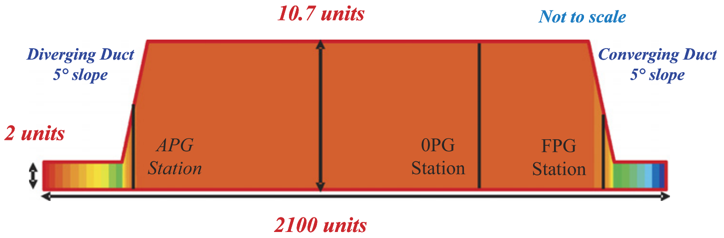

Fig. 5. Computational domain showing the approximate stations for extracting favorable (FPG), zero (ZPG), and adverse (APG) pressure-gradient RANS data (colored by static pressure).

We generate the RANS solutions using an in-house code, UNCLE-TF (Zierke, 1997). The code has been validated for internal-flow configurations and has been used extensively for Navy propulsor-design work. UNCLE-TF solves the mean momentum and mass conservation budgets. The turbulence closure uses the two-equation $q{-}\omega$ turbulence model with near-wall damping; q is a turbulence velocity scale interpreted as the square-root of the turbulence kinetic energy, and ω is an inverse turbulence time scale related to turbulence dissipation. Mesh density in the supporting grid uses 131 grid points across the channel and 439 grid points in the flow direction. Sublayer resolution is targeted. The near-wall spacing of the grid achieves a $y^+ \equiv u_* y/\nu$ value for the first grid point away from the wall of between 0.25 and 0.5; the friction velocity u_* is defined by $u_* \equiv \sqrt{\tau_w/\rho}$ where τ_w is the wall shear stress.

The zero pressure gradient results are extracted from the recovery stage of the numerical simulation. The recovery section is sufficiently long that fully-developed channel flow is achieved prior to entering the contraction. The Reynolds number of the simulation is chosen based on the best match between the zero-pressure gradient RANS results and Schloemer's data. The adverse and favorable pressure gradient stations are chosen where the boundary-layer parameters and the peak in the turbulent kinetic energy, are in reasonable agreement with Schloemer (1966, 1967).

Table 2 compares boundary-layer statistics from Schloemer to the extracted RANS results. The agreement is good for the length scale and skin friction data. The largest deviation is in the first shape factor (the ratio of the boundary-layer thickness to the displacement thickness) for the zero pressure gradient case. Schloemer reports a value near 7. The RANS data yield a value near 9. However, the magnitudes of the dimensionless surface-pressure gradients differ from Schloemer's measurements. We were not able to match all of Schloemer's parameters exactly while choosing profiles to extract from the RANS solution; therefore, we favored agreement with the length scale and skin friction data because they are strongly related to the velocity profile and its gradients, data that have a significant impact on the model results. Because the pressure gradient is not used in our modeling, we relaxed our requirements on matching this parameter.

Also presented in Table 2 are values for the boundary-layer edge velocity, the friction velocity, and the boundary-layer thickness, displacement thickness, and momentum thickness nondimensionalized by the entrance channel half-height and centerline velocity. These data provide a complete disclosure of the mean flow field characteristics to facilitate conversion between nondimensionalizations and recovery of dimensional results, if desired.

Mean-velocity profiles are presented in Fig. 6. The solid lines are from RANS and Schloemer's data are the symbols. The agreement is good. The largest deviation is for the zero-pressure-gradient case, consistent with the reported difference in the first shape factor. The mean-velocity data in wall coordinates are presented in Fig. 6(b). The zero pressure gradient case follows the universal profile and shows a well developed logarithmic region. The adverse- and favorable-pressure gradient cases are close to the universal curve for the inner region of the boundary layer but deviate in the outer flow, where the adverse pressure gradient exceeds the zero pressure-gradient one while the favorable pressure-gradient profile undershoots the zero-pressure gradient result.

Turbulence data from RANS are presented in Fig. 7. The dimensionless turbulence length scale, Fig. 7(a), for the $q{-}\omega$ model is defined as $\ell \equiv \beta q/\omega$, where β, the proportionality constant, is observed to be between 0.54 and 0.65 (0.54

Table 2
Summary of the boundary-layer parameters for Schloemer's adverse, favorable, and zero pressure gradient data compared to the RANS results

	Favorable			Zero			Adverse		
	Schloemer	Schloemer	RANS	Schloemer	Schloemer	RANS	Schloemer	Schloemer	RANS
Re_θ	1340	1470	1414	4500	5800	5041	7380	9180	8631
δ/δ_*	12.900	14.700	11.527	6.950	6.970	9.241	4.860	4.860	4.494
δ_*/θ	1.350	1.390	1.292	1.345	1.340	1.266	1.577	1.585	1.493
C_f	470×10^{-3}	4.50×10^{-3}	4.91×10^{-3}	3.10×10^{-3}	3.00×10^{-3}	3.60×10^{-3}	1.82×10^{-3}	1.76×10^{-3}	1.86×10^{-3}
$(\theta/\tau_w)\mathrm{d}P/\mathrm{d}x$	−0.128	−0.216	−0.364			−0.058	2.120	2.070	3.420
u_e			0.545			0.201			0.227
u_*			2.70×10^{-2}			8.51×10^{-3}			6.93×10^{-3}
δ			0.552			4.199			3.637
δ_*			0.048			0.454			0.809
θ			0.037			0.359			0.542
Re_δ			21 061			58971			57 892
Re_*			90			271			393
Re			70 000			70000			70 000

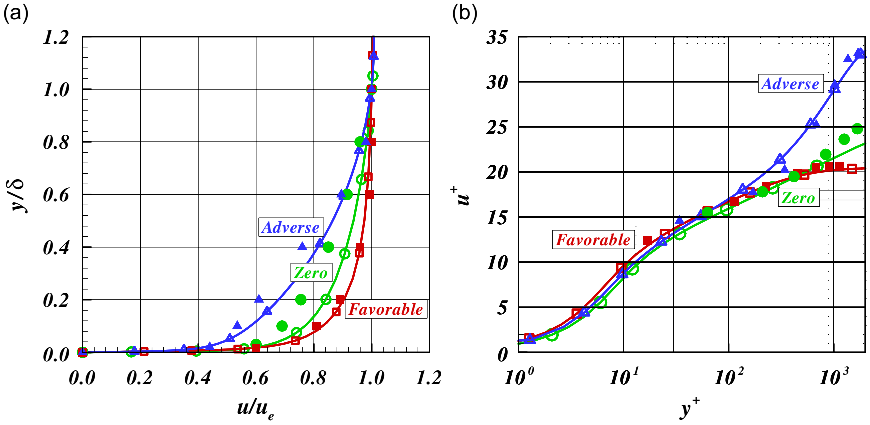

Fig. 6. Mean-velocity profiles: (a) compared to Schloemer's data and (b) in wall coordinates. Open symbols are simulations; closed symbols are Schloemer's measurements. ○, zero pressure gradient; □, favorable pressure gradient; △, adverse pressure gradient.

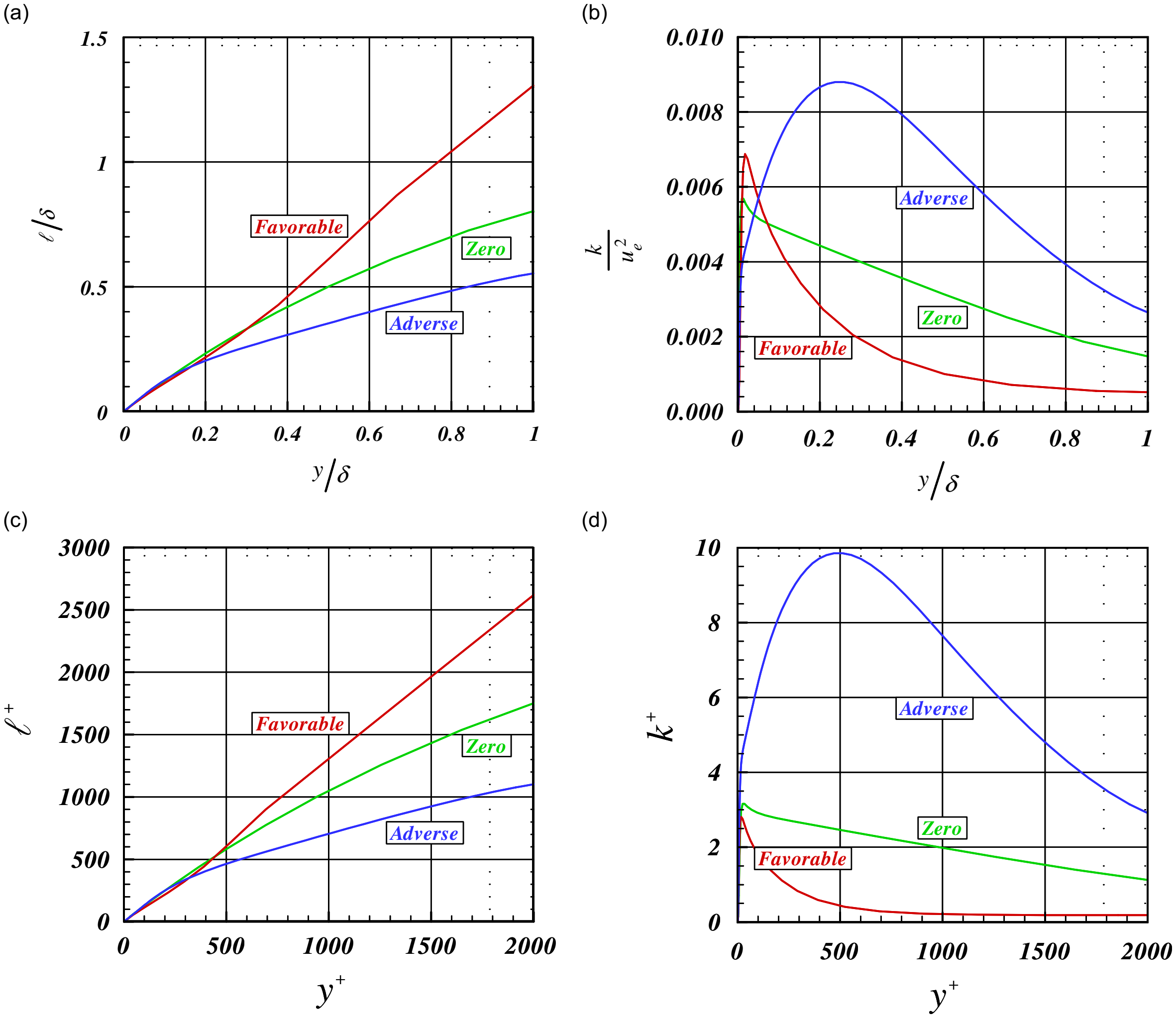

Fig. 7. Profiles of the turbulence correlation length (ℓ) and kinetic energy (k) from RANS: top panels normalized by the boundary layer depth (δ) and the velocity at δ (u_e) and the bottom panels in wall units.

is used for the current model). The dimensionless turbulence length scale shows an increasing trend from adverse to favorable pressure gradient. The data are nondimensionalized on the boundary-layer thickness, so the larger value for favorable pressure gradient reflects the thinning boundary layer for that case. The turbulence length scale for the adverse pressure gradient is physically longer, but the boundary-layer thickness is comparatively larger too.

Profiles of the turbulence kinetic energy (tke) are presented in Fig. 7b. Schloemer presents data for the streamwise root-mean-square (u_{rms}) value of velocity. The square of that statistic provides one component of the tke. The other components, though, are not reported, so a tke value cannot be recovered and a direct data comparison cannot be made. Schloemer's streamwise-velocity r.m.s. values for the favorable and zero pressure-gradient cases peak very close to the wall. The RANS results do as well. His adverse pressure-gradient data show a peak in the u_{rms} profile near y/δ of 0.2, as do the RANS tke results. Our experience shows that the predicted surface-pressure variance is sensitive to the location of the peak in the tke profile meaning that matching this location is as important as matching the other boundary-layer statistics in extracting a validation data set.

3.2. Numerical integration

The terms contributing to the turbulent boundary-layer surface-pressure spectrum are sufficiently complicated that an analytic solution to (11) is unlikely. Instead, the convolution is evaluated using numeric integration over an integration volume sufficiently large to approximate an infinite domain. The source terms are function of the distance to the nearest wall, so this coordinate direction is treated separately in the numeric integration. We compute the horizontally integrated source terms for each cell in the wall normal direction and sum the contributions. To integrate the horizontal directions in physical space and all directions in correlation space, we use discrete Gauss–Legendre integration which should provide optimum efficiency for smooth functions. The discrete evaluation of the convolution replaces the integrals with summations of the source terms at specified locations weighted by appropriate weighting functions

$$\begin{aligned}\frac{1}{\rho^2}R_{pp}(\Delta\vec{x}_s,\Delta t) &= \int_{\vec{x}}\int_{\vec{r}}(SRC_{\mathrm{TMS}}+SRC_{\mathrm{TTN}}+SRC_{\mathrm{TTM}}+SRC_{\mathrm{TTS}})\,\mathrm{d}\vec{r}\,\mathrm{d}\vec{x}\\ &\approx \sum_{\vec{x}}\sum_{\vec{r}}(SRC_{\mathrm{TMS}}+SRC_{\mathrm{TTN}}+SRC_{\mathrm{TTM}}+SRC_{\mathrm{TTS}})W_{\vec{x},\vec{r}}\Delta\vec{r}\Delta\vec{x}. \end{aligned} \tag{22}$$

Values for the integration locations and for the applied weights are returned from the Gauss–Legendre integration subroutine, GAULEG, from Press et al. (1988).

3.3. Validation results

Integrand and cumulative results for the surface-pressure variance, $R_{pp}(\vec{0},0)/\rho^2$, are presented in Fig. 8, nondimensionalized by inner variables. The variance (black) is the sum of the *TMS* (red)[1] color is used only in the web-version of the paper and *TTN* (green) contributions. The *TTM* (blue) and *TTS* (orange) profiles are shown to have negligible effect. One sees in the data an increasing contribution from the outer part of the boundary layer and from the *TTN* term in the transition from favorable to adverse pressure gradient. The *TMS* term consistently has a local maximum in the neighborhood of $y^+ = 10$–12 and decays at intermediate distances. The *TTN* term becomes pronounced at intermediate distances. In the outer boundary layer for the adverse pressure-gradient case, a second peak in the *TMS* term is observed and the *TTN* term remains significant for most of the boundary layer. The significant change in the *TMS* and *TTN* behaviors across the boundary layer with pressure gradient would be difficult to capture in general with *ad hoc* models.

The integrand profiles in Fig. 8 suggest the existence of two separate contributions, one from the inner layer and a second from the outer layer. The inner layer contribution is common for each of the pressure gradients. The outer layer contribution is absent from the favorable pressure gradient case, is evident under zero-pressure gradient, and is pronounced for the adverse pressure-gradient condition. The existence of inner- and outer-layer scaling contributions to surface-pressure spectra exists in the literature [see Goody and Simpson (2000) for an overview].

The surface-pressure covariances for the favorable, zero, and adverse pressure gradient cases are presented in Fig. 9. The color scheme is consistent with Fig. 8. The favorable pressure gradient case is characterized by a smaller correlation than the zero and adverse pressure-gradient cases, and significant contributions are bounded to a smaller band of time separations. The zero and adverse pressure gradient correlations are significant over a wider band of time separations.

---

[1] Color is used only in the web-version of the paper.

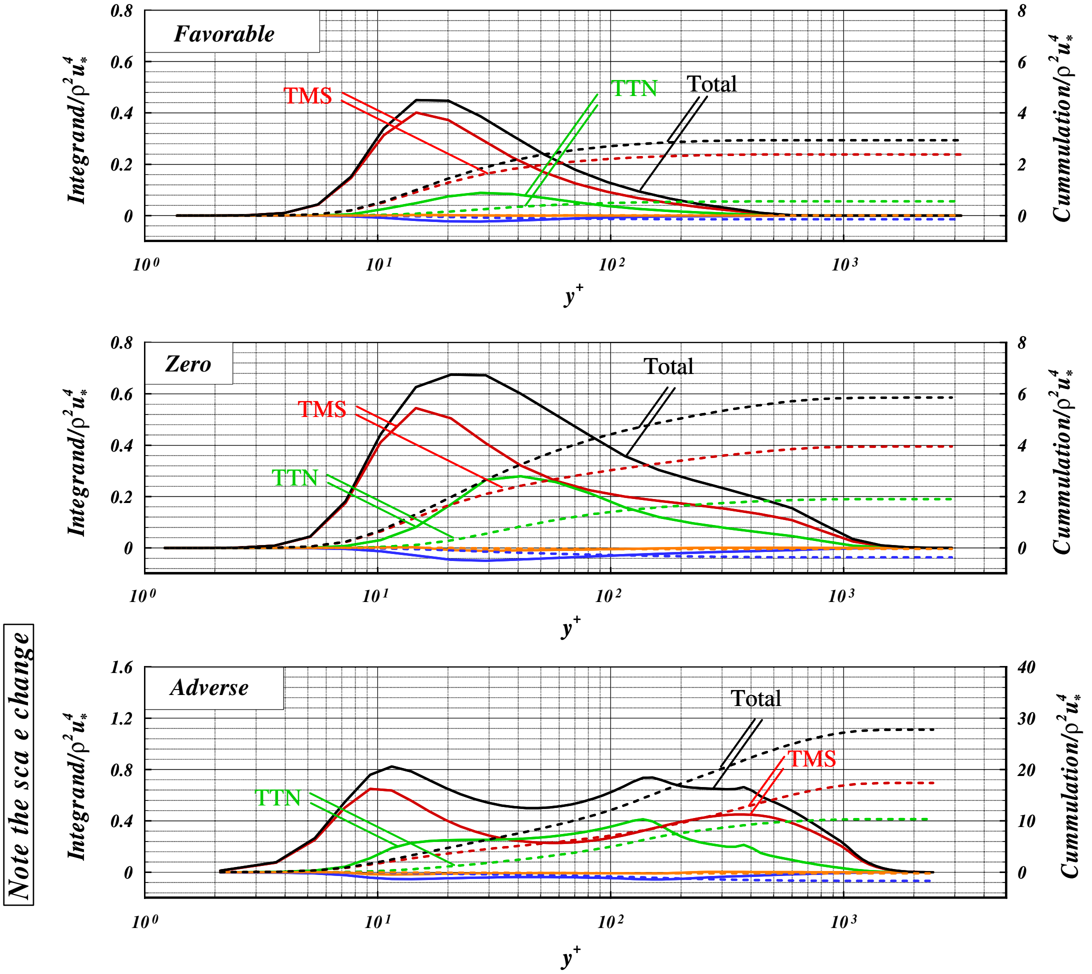

Fig. 8. Integrand (solid) and cumulative (dashed) contributions to the surface-pressure variance in wall coordinates: TTM is slightly negative, and TTS is near zero.

The adverse pressure gradient case, though, has markedly greater correlations, a factor of ~6 higher than the zero and favorable pressure-gradient cases. For each case the TMS contribution is dominant, however, one sees again the TTN term plays an increasing role in the transition from favorable to adverse pressure gradient.

The TMS term depends on the C^{22} correlation coefficient whose correlation volume is not inclined to the flow, thus the TMS term is symmetric around zero separation time. The asymmetries in C^{11} and C^{33} with separation time are significantly impressed on the TTN profiles, as one sees a preference for negative time separations.

Components of the surface-pressure spectra are presented in Fig. 10. Neither the TTM nor the TTS contributions are significant. The primary contribution is from TMS interactions for all cases. The TTN contribution has an increasing importance with decreasing pressure gradient.

The total spectra are replotted in Fig. 11 with Schloemer's data overlayed as symbols. The low-frequency levels of the predicted spectra agree well with Schloemer's. One observes the increasing amplitude of the spectra at low frequency with the trend from favorable to adverse pressure-gradient and a tendency to return to a common high frequency tail under inner-variable scaling. The collapse at high frequencies is also reported in the literature. Goody and Simpson (2000) provide an overview. The separate inner/outer layer contributions to the wall-pressure spectrum are observed in these data: note the roll-offs near 0.03 and 0.4 for the zero and adverse pressure gradient cases. Presumably the low frequency roll-off is associated with outer-layer activity, while the high frequency roll-off is associated with the inner-layer contributions. The double roll-off character is not seen as readily in the favorable pressure-gradient case, in agreement with the observation from Fig. 8 that the outer-layer is largely inactive for this case.

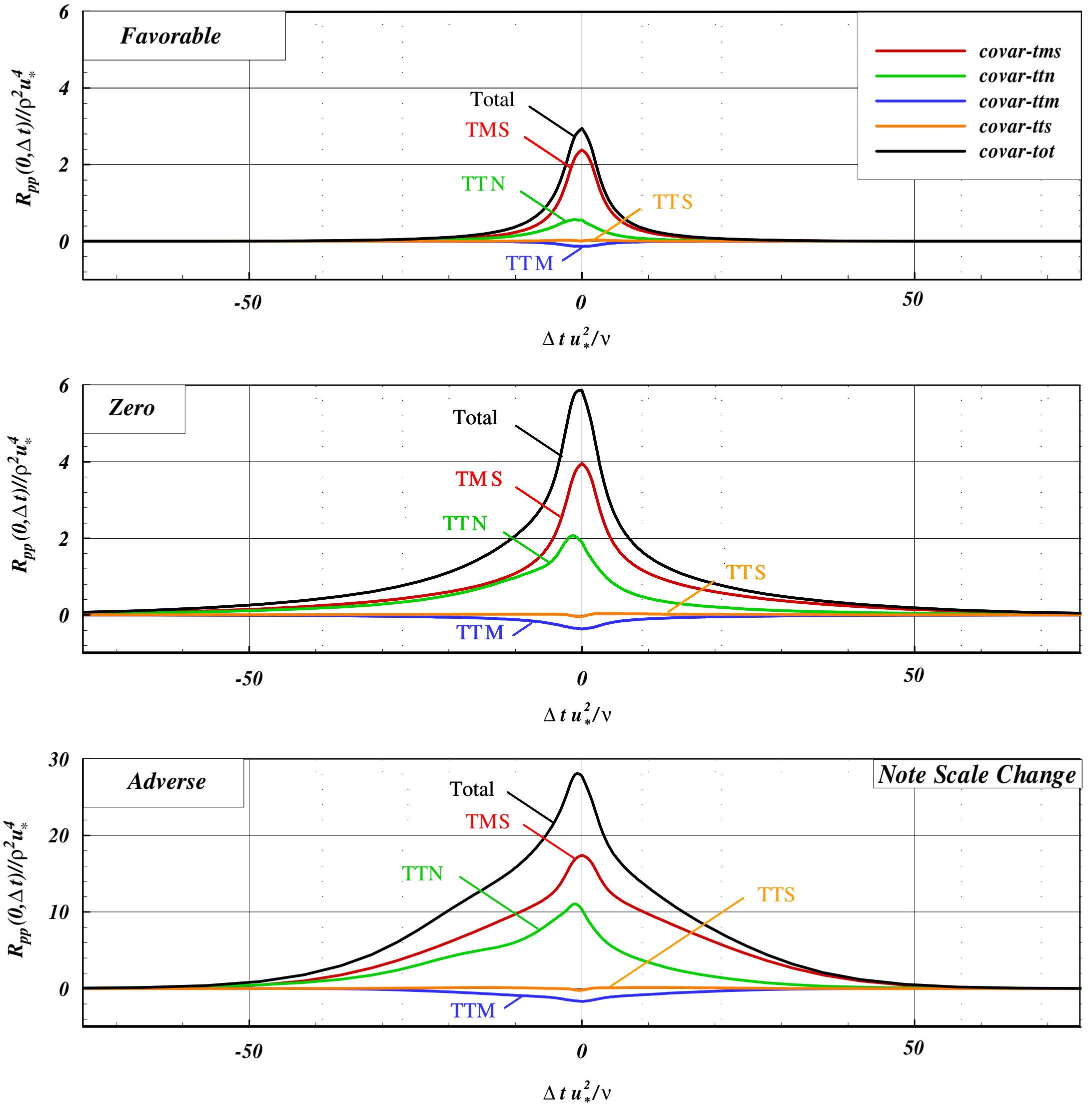

Fig. 9. The surface-pressure correlation function vs. separation time for favorable, zero, and adverse pressure-gradient conditions.

The outer-layer is much more active in the adverse pressure-gradient case, accounting for the significantly enhanced spectral levels at low frequencies. The dip in the adverse pressure-gradient spectrum at intermediate frequencies suggests that the inner-layer and outer-layer contributions may be independent. This behavior for intermediate frequencies is not observed in Schloemer's data. One could infer a mild dip in the results presented by Goody and Simpson (2000).

The model predictions at zero pressure gradient show an extensive ω^{-1} regime not seen in Schloemer's data. This regime is associated with the logarithmic zone of the turbulent boundary layer (Gravante et al., 2000). An extensive logarithmic layer is clearly observed in Fig. 6 for the RANS results. The RANS velocity profile matches the universal profile very well. The noticeable difference in Fig. 6 between the RANS mean-velocity profile and Schloemer's data indicates that Schloemer's boundary layer does not exhibit a similarly extensive logarithmic zone, and this explains the difference at intermediate frequencies between the RANS-based predictions and Schloemer's measurements.

The agreement with the favorable pressure-gradient data is reasonable though the low frequency amplitude is underpredicted. The high-frequency tail of Schloemer's favorable pressure-gradient data is offset from the zero and adverse pressure-gradient cases. His favorable-pressure gradient data required significant probe volume corrections over the entire frequency range because the boundary layer was very thin. A final assessment of the surface-pressure spectrum model will require additional experimental data-sets or possibly high-Reynolds-number Direct Numerical

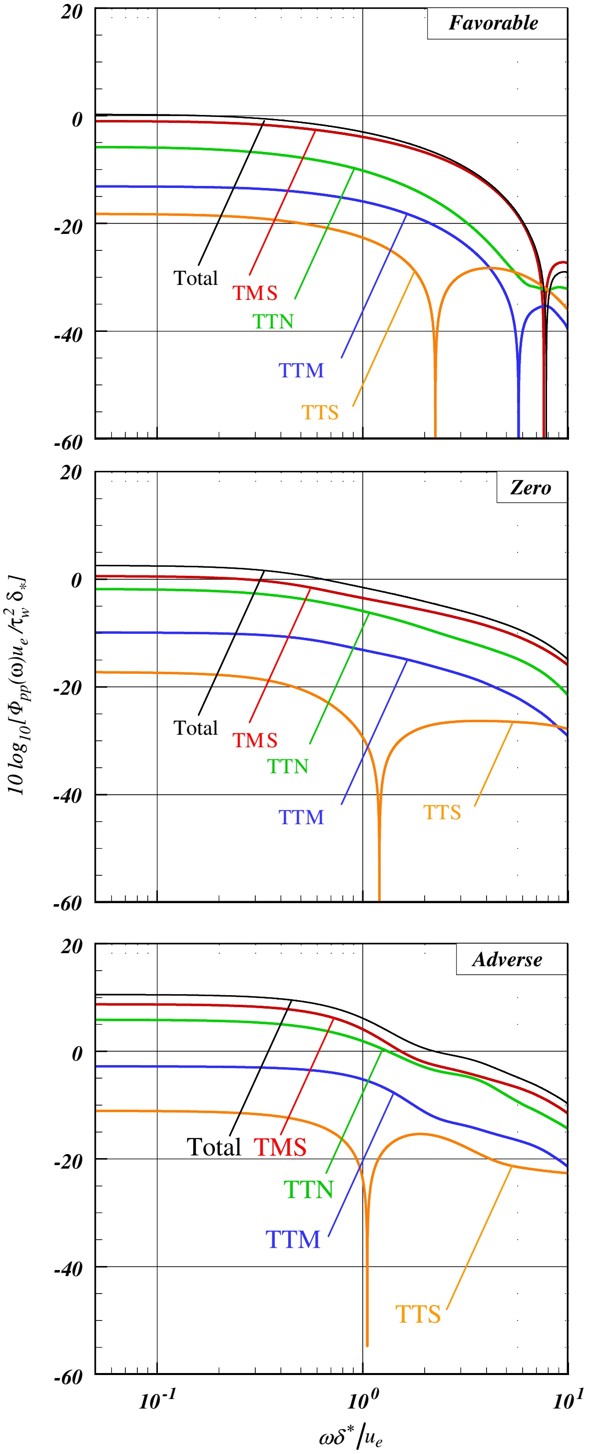

Fig. 10. The surface-pressure spectra for favorable, zero, and adverse pressure-gradient conditions. “Total” is the sum TMS + TTN.

Simulations (DNS) or Large-Eddy Simulations (LES); see Choi and Moin (1990) and Chang et al. (1999). Of particular interest is the structure of the turbulence-velocity correlation functions in the inner and intermediate layers of the turbulent boundary layer.

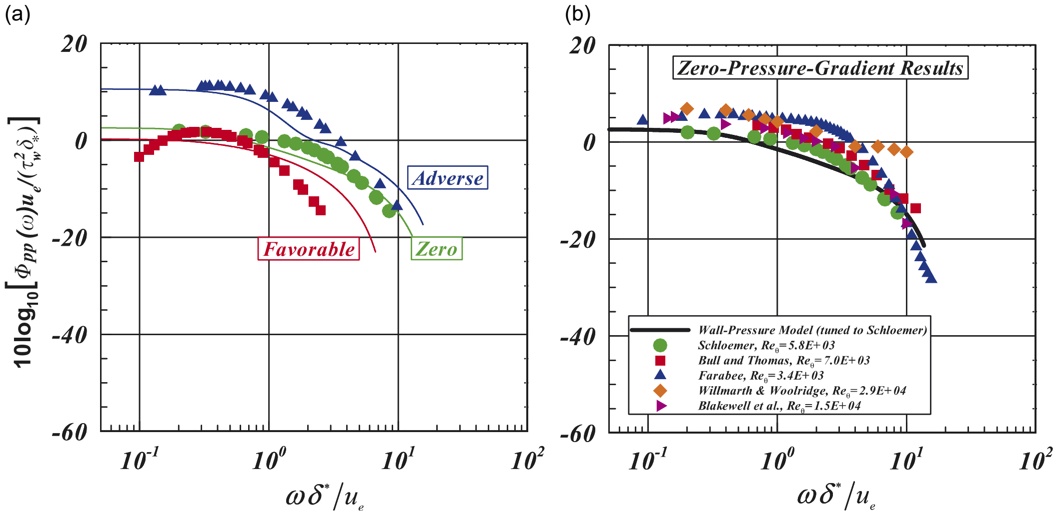

Fig. 11. Predicted surface-pressure spectra (lines) compared to (a) Schloemer's data (symbols) for favorable (square), zero (circle), and adverse (triangle) pressure gradients and (b) the Bull and Thomas, Farabee, Schloemer, Willmarth and Woodrigde, and Blakewell zero pressure gradient data-sets.

4. Summary and conclusions

A stochastic model for the surface-pressure covariance and associated wavenumber-frequency spectrum has been developed that uses RANS data as input. The model development begins with the exact equation for the surface-pressure covariance then closes the expression with boundary-layer-specific assumptions. This foundation permits the coupled model to respond to local geometry and flow complications through the fluids solver, exploiting the maturity that RANS turbulence closures have gained over decades of development. Contemporary RANS models are used for bow to stern simulations of ships, to predict flow effects from detailed features on aerospace vehicles, for multi-component modeling of engines, and for many other purposes. In principle, the coupled model inherits this flexibility.

Validation against the data-set reported by Schloemer for surface-pressure frequency spectra under favorable, zero, and adverse pressure gradients shows that the model appears to predict wall-pressure spectra well for the range of Reynolds numbers reported by Schloemer and responds appropriately to pressure gradients. The importance of considering both turbulence mean-shear interactions and turbulence normal-stress interactions individually is clearly illustrated. Both contribute significantly but respond strongly to different parts of the turbulent boundary layer.

The contributions to the TBL wall-pressure autospectra from the TMS and TTN terms throughout the boundary layer agree with qualitative observations made in the literature (Schloemer, 1966, 1967; Goody and Simpson, 2000; Gravante et al., 2000), but might be validated further using time accurate solutions of turbulent flow fields using tools like Direct Numerical Simulation (DNS) or Large Eddy Simulation (LES). Computations such as those made by Choi and Moin (1990) and Chang et al. (1999) are available, and attempt to show the correlation of wall pressures to turbulent structures in the boundary layer. Unfortunately, the simulations are for very low Reynolds numbers (3200 based on the channel half-width). When computational resources allow for time accurate CFD tools to generate solutions for flow fields at reasonably high Reynolds numbers, the model presented here could be further validated.

Further validation of the RANS-based model would benefit from data for stronger adverse and favorable pressure gradients. Favorable pressure-gradient measurements would have the most benefit, because the fidelity of the model comparison to Schloemer's favorable pressure-gradient case was less clear. Comparisons to data for 3-D boundary layers are also warranted. Validation data for airfoil sections or in pipe elbows near regions of high pressure gradients are examples.

Finally, a validation of the complete wavenumber-frequency spectrum has not yet been attempted. Comparisons of the new model for the surface-pressure wavenumber-frequency spectrum to existing models documented by Graham (1997) at zero-pressure gradient, along with the data of Cipolla and Keith (2000) derived from the measurements of Schloemer (1967) in favorable and adverse pressure gradients are planned as follow-on work. We also hope to compare space–time variations of wall-pressure fluctuations to the DNS results of Na and Moin (1998) in adverse pressure gradients.

Acknowledgments

The authors would like to thank the Office of Naval Research under ONR Contract N00014-00-G-0058, monitored by Lynn Peterson. The authors would like to also acknowledge contributions from Dr Charles Knight who developed an earlier model for a RANS-based turbulent boundary-layer forcing-function tool that motivated this work.

References

Blake, W.K., 1986. Mechanics of Flow-induced Sound and Vibration. Academic Press, New York.

Bull, M.K., 1996. Wall pressure fluctuations beneath turbulent boundary layers: some reflections on forty years of research. Journal of Sound and Vibration 190, 299–315.

Chang, P.A., Piomelli, U., Blake, W.K., 1999. Relationship between wall pressure and velocity field sources. Physics of Fluids 11, 3434–3448.

Chase, D.M., 1980. Modeling the wavevector-frequency spectrum of turbulent boundary layer wall pressure. Journal of Sound and Vibration 70, 29–67.

Chase, D.M., 1987. The character of turbulent wall pressure spectrum at subconvective wavenumbers and a suggested comprehensive model. Journal of Sound and Vibration 112, 125–147.

Choi, H., Moin, P., 1990. On the space–time characteristics of wall-pressure fluctuations. Physics of Fluids 2, 1450–1460.

Cipolla, K., Keith, W., 2000. Effects of pressure gradients on turbulent boundary layer wave number frequency spectra. AIAA Journal 38, 1832–1836.

Corcos, G.M., 1963. Resolution of pressure in turbulence. Journal of the Acoustical Society of America 35, 192–199.

Gardner, S., 1965/1966. On surface pressure fluctuations produced by boundary layer turbulence. Acoustica 16, 67–74.

Gavin, J.R., 2002. Unsteady forces and sound caused by boundary layer turbulence entering a turbomachinery rotor. Ph.D. Thesis, The Pennsylvania State University, University Park, PA.

Goody, M.C., 2002. An empirical model of surface-pressure fluctuations that includes Reynolds number effects. AIAA-2002-2565.

Goody, M.C., Simpson, R.L., 2000. Surface pressure fluctuations beneath two- and three-dimensional turbulent boundary layers. AIAA Journal 38, 1822–1831.

Graham, W.R., 1997. A comparison of models for the wavenumber-frequency spectrum of turbulent boundary layer pressures. Journal of Sound and Vibration 206, 541–565.

Gravante, S.P., Naguib, A.M., Wark, C.E., Nagib, H.M., 2000. Characterization of the pressure fluctuations under a fully developed turbulent boundary layer. AIAA Journal 36, 1808–1816.

Keith, W.L., Hurdis, D.A., Abraham, B.M., 1991. A comparison of turbulent boundary layer wall pressure spectra. ASME NCA-Vol. 11/FED-Vol. 130, Flow Noise Modeling, Measurement and Control.

Kim, J., 1989. Structure of pressure fluctuations in turbulent channel flow. Journal of Fluid Mechanics 205, 421–451.

Klebanoff, P.S., 1954. Characteristics of turbulence in a boundary layer with zero pressure gradient. NACA Technical Note 3178.

Kraichnan, R.H., 1956. Pressure fluctuations in turbulent flow over a flat plate. Journal of the Acoustical Society of America 28, 378–390.

Laufer, J., 1950. Investigation of the turbulent flow in a two-dimensional channel. NACA Technical Note 2123.

Laufer, J., 1954. The structure of turbulence in fully developed pipe flow. NACA Report 1174.

Meecham, W.C., Tavis, M.T., 1980. Theoretical pressure correlation functions in turbulent boundary layers. Physics of Fluids 23, 1119–1131.

Na, Y., Moin, P., 1998. The structure of wall-pressure fluctuations in turbulent boundary layers with adverse pressure gradient and separation. Journal of Fluid Mechanics 377, 347–373.

Press, W.H., Flannery, B.P., Teukolsky, S.A., Vetterling, W.T., 1998. Numerical Recipes. Cambridge University Press, Cambridge.

Schloemer, H.H., 1966. Effects of pressure gradients on turbulent boundary-layer wall-pressure fluctuations. USL Report No. 747, US Navy Underwater Sound Laboratory, Fort Trumbull, New London, Connecticut, July 1.

Schloemer, H.H., 1967. Effects of pressure gradients on turbulent boundary layer wall pressure fluctuations. Journal of the Acoustical Society of America 42, 93–113.

Smolyakov, A.V., Tkachenko, V.M., 1991. Model of a field of pseudosonic turbulent wall pressures and experimental data. Soviet Physics—Acoustics 37, 627–631.

Townsend, A.A., 1980. The Structure of Turbulent Shear Flow, second ed. Cambridge University Press, New York.

Zierke, W.C. (Ed.), 1997. A physics-based means of computing the flow around a maneuvering underwater vehicle. Technical Report No. TR97-002, ARL/Penn State University, January 1997.